Observational constraints on the ultrahigh energy cosmic neutrino flux from the second flight of the ANITA experiment

P. W. Gorham,[1] P. Allison,[1] B. M. Baughman,[2] J. J. Beatty,[2] K. Belov,[3] D. Z. Besson,[4] S. Bevan,[5] W. R. Binns,[6] C. Chen,[7] P. Chen,[7] J. M. Clem,[8] A. Connolly,[5] M. Detrixhe,[4] D. De Marco,[8] P. F. Dowkontt,[6] M. DuVernois,[1] E. W. Grashorn,[2] B. Hill,[1] S. Hoover,[3] M. Huang,[7] M. H. Israel,[6] A. Javaid,[8] K. M. Liewer,[9] S. Matsuno,[1] B. C. Mercurio,[2] C. Miki,[1] M. Mottram,[5] J. Nam,[7] R. J. Nichol,[5] K. Palladino,[2] A. Romero-Wolf,[1] L. Ruckman,[1] D. Saltzberg,[3] D. Seckel,[8] G. S. Varner,[1] A. G. Vieregg,[3] and Y. Wang[7]

[1]*Department of Physics and Astronomy, University of Hawaii, Manoa, Hawaii 96822, USA*
[2]*Department of Physics, Ohio State University, Columbus, Ohio 43210, USA*
[3]*Department of Physics and Astronomy, University of California Los Angeles, California 90095, USA*
[4]*Department of Physics and Astronomy, University of Kansas, Lawrence, Kansas 66045, USA*
[5]*Department of Physics and Astronomy, University College London, London, United Kingdom*
[6]*Department of Physics, Washington University in St. Louis, Missouri 63130, USA*
[7]*Department of Physics, National Taiwan University, Taipei, Taiwan*
[8]*Department of Physics, University of Delaware, Newark, Delaware 19716, USA*
[9]*Jet Propulsion Laboratory, Pasadena, California 91109, USA*

(Received 12 March 2010; published 16 July 2010)

The Antarctic Impulsive Transient Antenna (ANITA) completed its second Long Duration Balloon flight in January 2009, with 31 days aloft (28.5 live days) over Antarctica. ANITA searches for impulsive coherent radio Cherenkov emission from 200 to 1200 MHz, arising from the Askaryan charge excess in ultrahigh energy neutrino-induced cascades within Antarctic ice. This flight included significant improvements over the first flight in payload sensitivity, efficiency, and flight trajectory. Analysis of in-flight calibration pulses from surface and subsurface locations verifies the expected sensitivity. In a blind analysis, we find 2 surviving events on a background, mostly anthropogenic, of 0.97 ± 0.42 events. We set the strongest limit to date for 10^{18}–10^{21} eV cosmic neutrinos, excluding several current cosmogenic neutrino models.

DOI: 10.1103/PhysRevD.82.022004 PACS numbers: 98.70.Sa, 95.55.Vj, 95.85.Ry

I. INTRODUCTION

The existence of cosmic-ray particles of energies above 10^{19} eV, first established in the early 1960s, has become a problem of the first rank in particle astrophysics. Models for their production must generate particle energies many orders of magnitude higher than achievable on Earth, and these models in turn require extreme source physics that has not yet been formulated in a self-consistent manner. Even more problematic, the propagation of such particles is limited by strong energy loss due to the Greisen-Zatsepin-Kuzmin (GZK) process [1]. Hadrons are produced via the Delta-photoproduction resonance by interactions with cosmic microwave background (CMB) photons. This GZK cutoff in energy limits the propagation distance of the ultrahigh energy cosmic rays (UHECRs) to within 100–200 Mpc in the current epoch, and severely distorts the observed energy spectrum. Astronomy using charged-particle UHECRs is thus limited to the local universe, suffering from both the loss of source spectral information, and the difficulty in back-tracing UHECRs through intergalactic magnetic fields.

At distances of several Gpc, corresponding to the star-formation maximum at redshift $z \sim 1$, the higher energy and density of the CMB photons leads to even greater restrictions on cosmic-ray propagation, and a more rapid energy loss to Delta photoproduction. However, information about the source particles does survive in the form of secondary neutrinos in the decay chain, known as the ultrahigh energy (UHE) cosmogenic neutrinos, first described by Berezinsky and Zatsepin (BZ) [2]. Their momenta are unaffected by magnetic fields, and they propagate without energy loss directly to Earth, retaining information about the cosmic distribution of UHECRs and their sources.

The ANITA Long Duration Balloon experiment was designed to search for cosmogenic neutrinos via electromagnetic cascades initiated by the neutrinos in Antarctic ice, the most massive body of accessible, solid, radio-transparent dielectric material on Earth. We previously placed limits on the UHE cosmic neutrino flux from the first flight of ANITA [3], and provided a separate detailed description [4] of the ANITA instrument, flight system, data acquisition, and analysis methods. In this article we detail upgrades and augmentations beyond the instrument and methodology previously reported.

II. EXPERIMENTAL TECHNIQUE

The second flight of ANITA (ANITA-II) launched from Williams Field, Antarctica on December 21, 2008 and landed near Siple Dome after 31 days aloft, resulting in

28.5 live days. Figure 1 shows an image of the payload on ascent after it had deployed to its full flight configuration, and an inset of the balloon and payload at float altitude. The mean ice depth in the field-of-view was 1.4 km, approximately one attenuation length at sub-GHz radio frequencies [5]. ANITA-II flew at an altitude of 35–37 km above sea level (33–35 km above the ice surface), and was thus able to synoptically view a volume of $\sim$1.6 M km^3 of ice. ANITA-II's sensitivity to cosmogenic neutrinos was improved substantially compared to ANITA-I: the front-end system noise temperature was reduced by 40 K, a 20% improvement in temperature [4]; 8 additional quad-ridged horn antennas were added to the previous total of 32; and the efficiency of the hardware trigger was optimized for impulsive signals. Also, the instrument was made much more robust to the effects of bursts of anthropogenic radio-frequency (RF) interference with the ability to mask channels from the trigger in the azimuthal sectors of the payload pointing at the noise source. Masking occurred on time scales of a minute. This upgrade significantly improved the live time when in view of strong sources such as McMurdo and Amundsen-Scott Stations, and trigger thresholds remained at thermal-noise levels throughout the flight. The combined effect of all of these modifications led to an increase of about a factor of 4 improvement in the expected signal from typical cosmogenic neutrino models as compared to ANITA-I.

FIG. 1 (color). The ANITA-II payload on ascent with the lower eight horn antennas deployed. The payload height is $\sim$8 m, and each antenna face is 0.95 m across. The inset shows the balloon and payload viewed telescopically at float altitude of 35 km.

The ANITA-II hardware trigger selects impulsive radio signals with broadband frequency content and temporal coherence over nanosecond time scales in the vertical polarization. The broadband nature of triggered signals was achieved by requiring power in multiple frequency bands, and temporal coherence was ensured by requiring impulsive power in a full-band channel. All simulations and laboratory measurements of Askaryan signals [6–8] from ice sheet neutrino interactions show that the RF signal at the payload is predominantly vertically polarized, due to the surface Fresnel coefficient and Cherenkov geometry [4,9]. No strict pulse shape requirements are enforced in the trigger to allow for variations in the shape of any individual neutrino-induced cascade, and the trigger is thus very inclusive. The trigger threshold rides at the ambient thermal-noise level to maintain an approximately constant trigger rate of $\sim$10 Hz, which is dominated (98.5%) by incoherent thermal-noise fluctuations. These thermal-noise triggers have well-modeled statistical probabilities for producing random impulses, and are highly suppressed in analysis with requirements of spatial and temporal coherence. Most other triggers are from anthropogenic sources. Such signals can mimic neutrinolike impulses, and may arise from high-voltage discharges in electrical equipment or from metallic structures charged by blowing snow or related effects. To remove such backgrounds, we identify active and prior human activity in Antarctica and optimize pointing resolution to reliably associate anthropogenic signals with known sources. We know of no expected particle-physics backgrounds.

Extensive calibration and validation of the system response and trigger efficiency for a range of impulse signal-to-noise ratios (SNRs) was done both prior to flight and with ground-to-payload impulse generating antennas during flight. These in-flight pulser systems were located at the launch site and at a remote field station at Taylor Dome on the edge of the Antarctic plateau. In both cases, impulse generators were fed through an antenna immersed in the ice as deep as 90 m [4]. In-flight measurements of the impulses from Taylor Dome provided validation that refraction effects on signal propagation through the ice surface do not significantly affect the coherence of the received signal, to distances of 400 km. Measurements of trigger efficiency in-flight were consistent with expectations from the ground calibrations, considering the narrower frequency content of impulses from Taylor Dome. Ground-to-payload signals provided an equally critical function in detector alignment and in determining the precision of directional reconstruction. ANITA's antenna signals are combined via pulse-phase interferometric methods [4], resulting in a radio map (''interferometric image'') for each polarization of the intensity as a function of payload elevation and azimuth. The largest peak in

either map determines the direction of the signal source. The payload coordinate frame is tied to the geodetic frame via onboard GPS and sun-sensor measurements to a precision of about 0.1°. The pointing resolution in our analysis is 0.2°–0.4° in elevation and 0.5°–1.1° in azimuth, depending on the SNR of the event.

III. DATA ANALYSIS

Our signal region comprises events that do not come from known sources of human activity (''camps'') and have no geospatial partner event within distance and angular separation criteria. We blinded the signal region in two ways simultaneously. First, we inserted an undisclosed number (12) of neutrinolike calibration events at random, concealed times throughout the flight. Second, we blinded ourselves to events in the signal region i.e. events that have no spatial partner. The analysis efficiency and background are estimated before opening this hidden signal box. Prior to unblinding, the complete set of in-flight calibration pulser data is used to optimize the pointing reconstruction of the analysis. In this section, we describe the sequence of analysis cuts that we applied to the sample until the final step, opening the blind signal box. Table I shows the total event sample, the sequential number of surviving events as each analysis cut is applied, and the efficiency of each cut. The number of *hardware-triggered events* is the total number of events recorded. *Quality events* exclude on- and off-payload calibration pulser events, unbiased autotrigger events, and a small fraction ($\sim 1\%$) of events with data corruption.

The great majority of remaining events are random thermal-noise-coincidence events in which individual waveforms are impulsive, but the ensemble of signals are incoherent and uncorrelated between antennas. We create an interferometric image in each polarization by cross-correlating waveforms from neighboring antennas and summing the total normalized cross-correlation value for each elevation and azimuth. We construct a ''coherently summed'' waveform given the direction of the largest peak in either map using the antennas that are closest to that peak. Figure 2 shows the vertical-polarization reconstruction position of all 21.2 M quality events. The color of each bin represents the average value of the peak of the interferometric image for events which fall in that bin. A value of <0.05 corresponds to the thermal-noise floor. The clear separation of thermal and anthropogenic events motivates our accounting for each background separately. Nearly all of the nonthermal excess will be removed in analysis because of its association with known bases.

Thermal-noise power originates from the ice and the electronics. Because thermal noise does not correlate between antennas, the peak in the interferometric image is equally likely to be in any direction. We establish thermal-noise cuts based on a sample of 2.1 M above-horizon (non-neutrino) events from a quiet period during the flight, when ANITA was not in view of McMurdo Station. To establish *reconstructed events*, we reject thermal noise by cutting on the peak value of the normalized cross-correlation in the interferometric image, the peak of the envelope of the coherently summed waveform, and its fraction of linear polarization. We also require that events reconstruct to locations where there is ice on the ground, down to 35° below horizontal. Using a modest extrapolation verified by simulation, we reject thermal-noise events at a level of $\leq 2.5 \times 10^{-8}$, corresponding to a background of 0.50 ± 0.23 events out of the 21.2 M quality events. The uncertainty represents a variation of fit parameters used for the extrapolation. For more detail, see Ref. [11]. Events which pass this set of cuts have been filtered for the presence of continuous-wave (CW) interference—typically narrow frequency-band signals from radio transmitters—and are largely impulsive in nature.

TABLE I. Event totals vs analysis cuts and estimated signal efficiencies for the Engel-Seckel-Stanev spectral shape [10].

Cut requirement	Passed		Efficiency
	Vpol	Hpol	
Hardware-triggered events	~26.7 M		...
(1) Quality events	~21.2 M		1.00
(2) Reconstructed events	320, 722		0.96
(3) Not traverses and aircraft	314, 358		1.00
(4) In Clusters <100 events	444		...
(5) Isolated singles	7	4	0.64
(6) Not misreconstructions	5	3	1.00
(7) Not of payload origin	2	3	1.00
Total efficiency			0.61

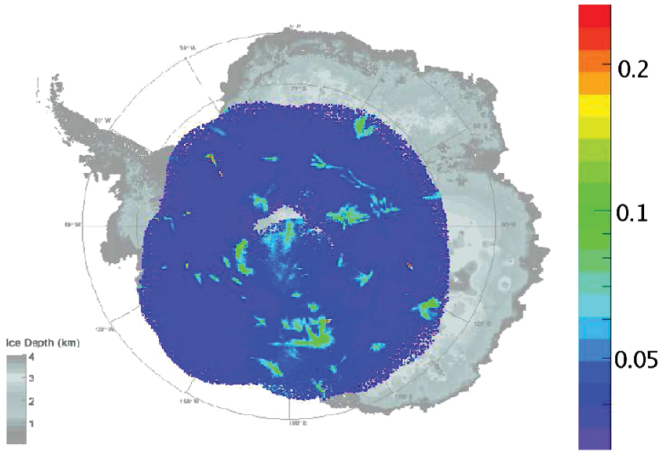

FIG. 2 (color). The vertical-polarization reconstruction position of all 21.2 M quality events, with the color scale representing the average peak value of the interferometric image for events which fall in that bin. The dark blue region is consistent with pure thermal noise. The green, yellow, and red regions are increasingly nonthermal and are consistent with anthropogenic noise.

Remaining events are mostly anthropogenic. To cut anthropogenic noise at a level of $\leq 3 \times 10^{-6}$, we require that any neutrino candidate be a single, geospatially-isolated event. It is extremely unlikely for two neutrino events to occur in close proximity to one another; correlated event locations are likely to indicate human activity. We first remove all events associated in both time and space with known flights and over-land traverses, so the remaining are *not traverses and aircraft*. We cluster all remaining events with known active and inactive camps, other events that also pass all previous cuts, and locations where low-level RF power has been detected by statistical correlation of weak signals, shown in Fig. 2. Events are clustered with a base or another event if the distance between the reconstructed location(s) is <40 km or if the angular separation between the locations is <5.5 times the pointing resolution for the event(s). Table II shows the number of clusters of reconstructed events vs cluster multiplicity for Clusters < 100 Events to give a sense of the distribution of anthropogenic noise, and is used to estimate the anthropogenic background contribution. Remaining unclustered events are *isolated singles*. The isolation requirement lowers acceptance since each event removes a region of the ice sheet around it from the available neutrino target volume. We used seven largely independent methods to estimate that the anthropogenic background remaining after our clustering cuts is 0.65 ± 0.39 vertically-polarized (Vpol) events and 0.25 ± 0.19 horizontally polarized (Hpol) events [11]. (For example, in Table II, there are 7 single events from known bases, 3 nonsingle clusters not from known bases, and 17 nonsingle clusters from known bases, yielding $3 \times 7/17 = 1.2$. After the polarization cut, this estimate becomes 0.91 in Vpol and 0.28 in Hpol. Combining this estimate with six other estimates that use a similar technique gives the quoted value and uncertainty.)

At this stage, the polarization angle of the event is calculated using the Stokes parameters, and the event is assigned to be Hpol ($< 40°$), Vpol ($> 50°$), or sideband ($40°$–$50°$). There were no events remaining in the sideband. Events that are *not misreconstructions* have a low probability of misreconstruction; we remove any event that clearly peaked at a sidelobe of the pattern in the interferometric image. This cut was tested using events from the ground-to-payload calibration pulsers and known camps. The requirement that events must be *not of payload origin* removes events associated with local interference originating on the payload but missed in the quality event stage; these are easily identified.

Upon opening the blind box, we first examine what happened to the 12 undisclosed, inserted neutrinolike events. Of the 12 inserted events, 11 were unique events with one duplicate event. Of the 11 unique events, 8 were Reconstructed Events, consistent with the calculated reconstruction analysis efficiency for such low-SNR events. Expected neutrino events have a wide range of SNR, but always at least as large as the inserted events.

TABLE II. Event cluster multiplicities for all clusters with fewer than 100 reconstructed events. All the cuts in Table I have been applied except for the isolated singles cut. The 5 events in the signal region correspond to the 2 + 3 events in the last entry in Table I.

Cluster multiplicity	Number of clusters	
	Camp	Not camp
10–100	8	1
5–9	7	1
4	1	0
3	0	0
2	1	1
1	7	5 (Signal region)

IV. RESULTS

After all cuts are applied, two events remain in the Vpol channel, and three in the Hpol channel. After clustering cuts, the thermal-noise background reduces to 0.32 ± 0.15 in each channel. The total background is 0.97 ± 0.42 events in the Vpol channel, and 0.67 ± 0.24 events in the Hpol channel. Thermal-noise backgrounds are likely reducible in future analysis. Figure 3 shows the reconstructed locations of the remaining events (large blue squares) on the Antarctic continent and the payload position at the time of detection (small black square connected to the blue square), along with camps (red points), and locations of low-level RF noise (black points).

All three Hpol events show characteristics which identify them as geo-synchrotron radio emission from UHECR air showers, reflecting from the ice surface (including sea

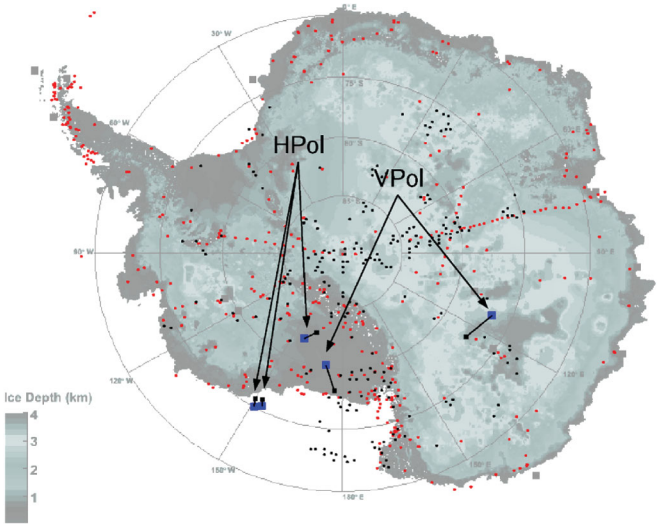

FIG. 3 (color). Events remaining after unblinding. The Vpol neutrino channel contains two surviving events. Three candidate UHECR events remain in the Hpol channel. Ice depths are from BEDMAP [28].

ice), as described in our ANITA-I results [12]. While ANITA-I saw 16 such events, the much smaller number of Hpol events seen in ANITA-II is due to the change of the trigger to favor Vpol events to maximize neutrino sensitivity.

The two remaining Vpol events are of unknown origin. In Fig. 4 we show some of the characteristics of these events, including the waveforms, frequency spectra, and interferometric images. Event 8381355 has been filtered using the adaptive filter developed for the analysis and is highly impulsive, with a nearly flat radio spectrum. Event 16014510 shows a central impulse with some additional distributed signal within 10–15 ns of the peak, and a frequency spectrum peaking near 400 MHz. The event still passes all cuts if the 400 MHz region is filtered by hand. The reconstructed directions are robust, supporting identification as isolated events. The waveforms and frequency spectra are within the range of simulated neutrino events. Both events are consistent in their locations and amplitudes with distributions of Monte Carlo-generated neutrinos. We lack adequate statistics to identify these two events as a unique nonanthropogenic population.

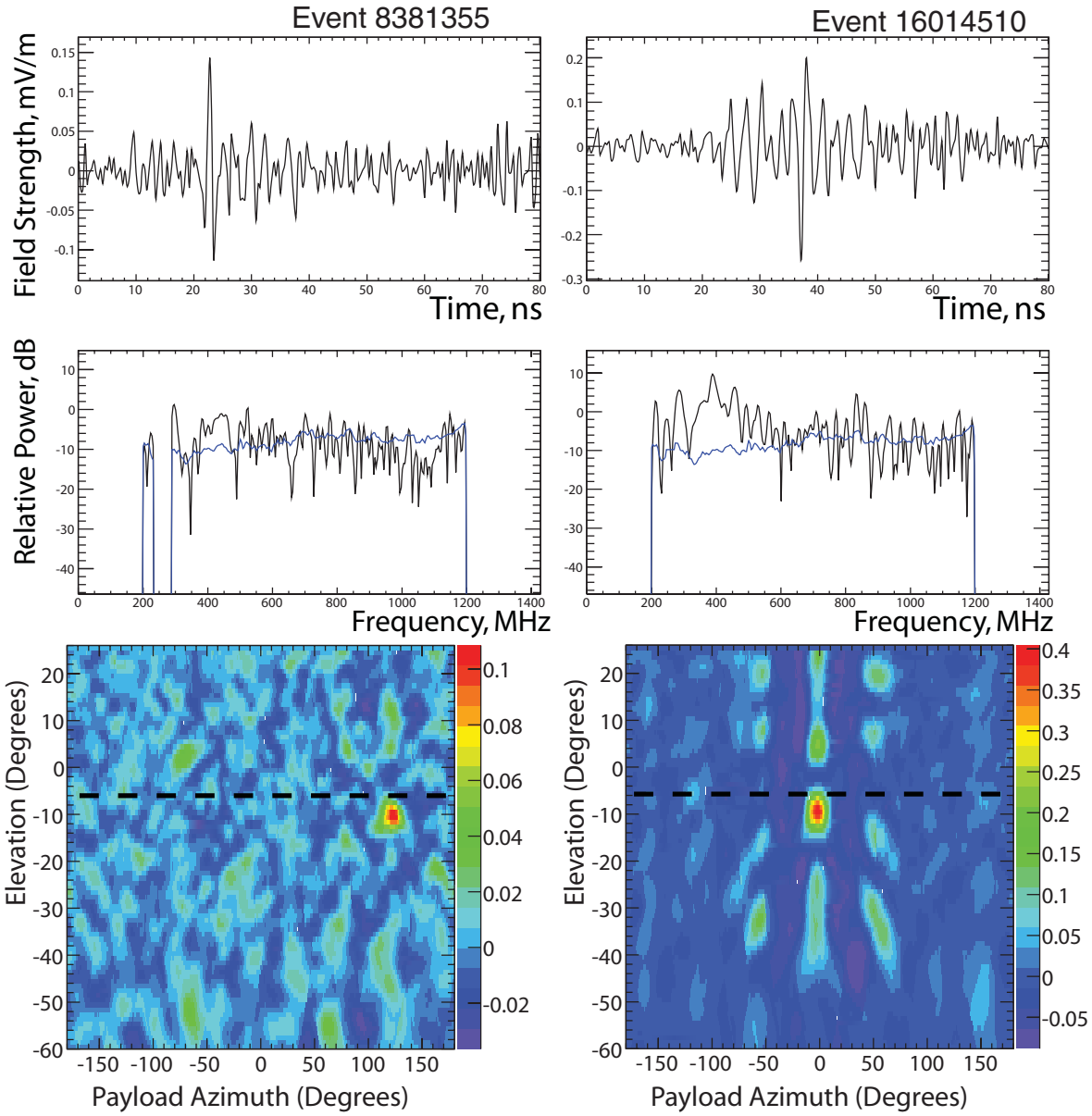

FIG. 4 (color). Top: Waveforms of incident field strength for the two surviving Vpol events. Event 8381355 is shown filtered between 235–287 MHz to remove weak continuous-wave noise. Middle: Corresponding frequency power spectra with an average thermal-noise spectrum shown in blue for reference. Bottom: Corresponding interferometric images showing the pulse direction. The dashed line is the horizon.

We proceed to set a limit including systematic errors [13]. The largest systematic error is on the acceptance, which is calculated using two independent Monte Carlo simulations [4]. The two simulations typically differ by 20%, which we take as a systematic error. The uncertainty on analysis efficiency includes two effects: statistical uncertainty on the efficiency calculation using calibration pulses, and a systematic error from the comparison of the efficiency on simulated neutrino events and calibration events. This uncertainty on analysis efficiency is 3%. The uncertainty on the background is discussed above. The inclusion of systematic errors only worsens the limit by about 10% because the procedure given in Ref. [13] accounts for both signs of systematic fluctuations.

Two other systematic sources are theoretical in nature. Changes in cross section, σ, can affect the limit in two ways: increasing the neutrino-nucleon cross section increases the interaction rate, but lowers the solid angle due to Earth shielding (and *vice versa*). The net result is an event rate which scales as $\sigma^{0.45}$. For a choice of cross section different than used here [14], our limit can be adjusted accordingly. Similarly, the event rate depends linearly on the Askaryan electric field [7]. Including reasonable variations on these parameters would affect the limit by $\sim$10%.

V. DISCUSSION

Our model-independent [15,16] 90% C.L. limit on neutrino fluxes is based on the 28.5 d live time, energy-dependent analysis efficiency ($68\% - 42\%$ from 10^{18}–10^{23} eV), the average acceptance from the two independent simulations [4,17], and 0.97 ± 0.42 expected background events including the systematic effects described above. Relative to the revised ANITA-I limit [3,18] shown in Fig. 5, the *expected* limit from this data, in the absence of signal, is a factor of 4 more sensitive. We set the *actual* limit, shown in Fig. 5, using our 2 observed candidates. Because ANITA-II saw more than the expected background, the actual limit is only a factor of 2 better than ANITA-I even though the *a priori* sensitivity is 4 times higher for ANITA-II. The ANITA-II limit supercedes the ANITA-I limit and would not significantly be improved by combining the results.

Table III gives integrated event totals for a range of cosmogenic neutrino models with widely varying assumptions. We also include for reference the expected number of events for a pure power-law neutrino spectrum that matches the Waxman-Bahcall flux bounds for both evolved and standard UHECR sources [27]. ANITA-II's constraint on cosmogenic neutrino models strongly excludes models with maximally energetic UHECR source spectra which saturate other available bounds [20,23,26]. These models generally assume very flat source energy spectra which may extend up to 10^{23} eV; our results are incompatible with a combination of both of these features. ANITA-II is

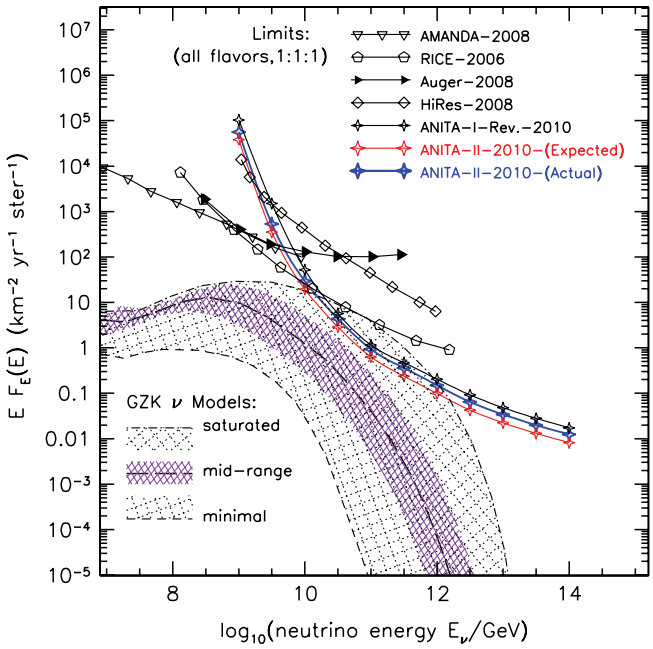

FIG. 5 (color). ANITA-II limit for 28.5 days live time. The red curve is the expected limit before unblinding, based on seeing a number of candidates equal to the background estimate. The blue curve is the actual limit, based on the two surviving candidates. Other limits are from AMANDA [29], RICE [30], Auger [31], HiRes [32], and a revised limit from ANITA-I [18]. The Berezinsky and Zatsepin (GZK) neutrino model range is determined by a variety of models [10,19–21,23,33,34].

TABLE III. Expected numbers of events N_ν from several cosmogenic neutrino models, and confidence level for exclusion by ANITA-II observations when appropriate.

Model and references	Predicted N_ν	C.L. %
Baseline models:		
Various [10,19–22]	0.3–1.1	···
Strong source evolution models:		
Aramo *et al.* 2005 [23]	2.6	78
Berezinsky 2005 [24]	5.4	97
Kalashev *et al.* 2002 [20]	5.9	98
Barger, Huber, and Marfatia 2006 [21]	3.6	89
Yuksel and Kistler 2007 [25]	1.8	···
Models that saturate all bounds:		
Yoshida *et al.* 1997 [26]	32	>99.999
Kalashev *et al.* 2002 [20]	20	>99.999
Aramo *et al.* 2005 [23]	17	99.999
Waxman-Bahcall fluxes:		
Waxman, Bahcall 1999, evolved sources [27]	1.5	···
Waxman, Bahcall 1999, standard [27]	0.52	···

now probing several models with strong source evolution spectra that are plausible within current GZK source expectations [20,21,23–25], some at >90% confidence level. The ANITA-II 90% C.L. integral flux limit on a pure E^{-2} spectrum for 10^{18} eV $\leq E_\nu \leq 10^{23.5}$ eV is $E_\nu^2 F_\nu \leq 2 \times 10^{-7}$ GeV cm^{-2} s^{-1} sr^{-1}. These differential and integral limits, as well as the individual model limits above, are the strongest constraints to date on the cosmogenic UHE neutrino flux.

ACKNOWLEDGMENTS

We thank the National Aeronautics and Space Administration, the National Science Foundation Office of Polar Programs, the Department of Energy Office of Science HEP Division, the UK Science and Technology Facilities Council, the National Science Council in Taiwan ROC, and especially the staff of the Columbia Scientific Balloon Facility.

[1] K. Greisen, Phys. Rev. Lett. **16**, 748 (1966); G. T. Zatsepin and V. A. Kuzmin, JETP Lett. **4**, 78 (1966).
[2] V. S. Beresinsky and G. T. Zatsepin, Phys. Lett. **28B**, 423 (1969).
[3] P. W. Gorham *et al.* (ANITA Collaboration), Phys. Rev. Lett. **103**, 051103 (2009).
[4] P. W. Gorham *et al.* (ANITA Collaboration), Astropart. Phys. **32**, 10 (2009).
[5] S. Barwick *et al.*, J. Glaciol. **51**, 231 (2005).
[6] G. A. Askaryan, Sov. Phys. JETP **14**, 441 (1962); **21**, 658 (1965).
[7] J. Alvarez-Muniz and E. Zas, Phys. Lett. B **411**, 218 (1997).
[8] D. Saltzberg *et al.*, Phys. Rev. Lett. **86**, 2802 (2001).
[9] P. W. Gorham *et al.* (ANITA Collaboration), Phys. Rev. Lett. **99**, 171101 (2007).
[10] R. Engel, D. Seckel, and T. Stanev, Phys. Rev. D **64**, 093010 (2001).
[11] A. Vieregg, Ph.D. dissertation, UCLA, 2010.
[12] S. Hoover *et al.* (ANITA Collaboration), arXiv:1005.0035 [Phys. Rev. Lett. (to be published)].
[13] G. Feldman and R. Cousins, Phys. Rev. D **57**, 3873 (1998); J. Conrad *et al.*, Phys. Rev. D **67**, 012002 (2003).
[14] Gandhi *et al.*, Astropart. Phys. **5**, 81 (1996).
[15] L. A. Anchordoqui *et al.*, Phys. Rev. D **66**, 103002 (2002).
[16] N. Lehtinen *et al.*, Phys. Rev. D **69**, 013008 (2004).
[17] The acceptance used from 10^{18}–10^{23} eV in half-decade energy steps is 4.3×10^{-4}, 5.0×10^{-2}, 0.92, 6.6, 36, 108, 259, 602, 1140, 1950, and 3110 km^2 − sr.
[18] S. Hoover, Ph.D. dissertation, UCLA, 2010.
[19] R. J. Protheroe and P. A. Johnson, Astropart. Phys. **4**, 253 (1996).
[20] O. E. Kalashev *et al.*, Phys. Rev. D **66**, 063004 (2002).
[21] V. Barger, P. Huber, and D. Marfatia, Phys. Lett. B **642**, 333 (2006).
[22] T. Stanev *et al.*, Phys. Rev. D **73**, 043003 (2006).
[23] C. Aramo *et al.*, Astropart. Phys. **23**, 65 (2005).
[24] V. Berezinsky, arXiv:astro-ph/0509675.
[25] H. Yuksel and M. D. Kistler, Phys. Rev. D **75**, 083004 (2007).
[26] S. Yoshida *et al.*, Astrophys. J. **479**, 547 (1997).
[27] E. Waxman and J. Bahcall, Phys. Rev. D **59**, 023002 (1998).
[28] M. B. Lythe, D. G. Vaughan *et al.* (BEDMAP Consortium), J. Geophys. Res. **106**, 11335 (2001).
[29] M. Ackermann *et al.* (IceCube Collaboration), Astrophys. J. **675**, 1014 (2008).
[30] I. Kravchenko *et al.*, Phys. Rev. D **73**, 082002 (2006).
[31] J. Abraham *et al.* (Pierre Auger Collab.), Phys. Rev. Lett. **100**, 211101 (2008).
[32] R. U. Abbassi *et al.* (HiRes Collab.), Astrophys. J. **684**, 790 (2008).
[33] O. E. Kalashev *et al.*, Phys. Rev. D **65**, 103003 (2002).
[34] M. Ave *et al.*, Astropart. Phys. **23**, 19 (2005).